Optical Materials 167 (2025) 117332

Contents lists available at ScienceDirect

Optical Materials

journal homepage: www.elsevier.com/locate/optmat

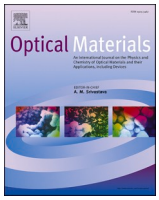

Research Article

Sputtered AlN/Al_2O_3 distributed Bragg reflectors on amorphous glass

Renjun Liu [a], Chandra Kant [a], Hüseyin Bilge Yağcı [b], Haifeng Qi [c], Hong Ji [a], William Solari [a], Sri Datta Aneesh Chodavarapu [a], Benxuan Li [d], Sheng Wang [b,e], Anthony J. Bennett [b], Ning Zhang [e], Ingo Ludtke [e], Wenlong Ming [b,e], Bo Hou [a,e,*]

[a] School of Physics and Astronomy, Cardiff University, Cardiff, CF24 3AA, United Kingdom
[b] School of Engineering, Cardiff University, Cardiff, CF24 3AA, United Kingdom
[c] School of Chemistry, Cardiff University, Cardiff, CF24 3AA, United Kingdom
[d] State Key Laboratory of Radio Frequency Heterogeneous Integration, Institute of Microscale Optoelectronics, Shenzhen University, Shenzhen, 518060, China
[e] Compound Semiconductor Applications Catapult, Newport, NP108BE, United Kingdom

ARTICLE INFO

Keywords:
Distributed bragg reflectors
AlN/Al_2O_3
Sputtering
Reflectance
Amorphous glass

ABSTRACT

With the sharp increase in the demand for vertical-cavity surface-emitting lasers (VCSELs), the need for high-performance and rapid thermal dissipation distributed Bragg reflectors (DBRs) has become significantly urgent in photonic and optoelectronic devices. In this work, a novel DBR composed of alternating aluminum nitride (AlN) and alumina (Al_2O_3) has been designed and prepared on an amorphous sodium silicate glass substrate via radio frequency (RF) sputtering technique. The effect of a number of stacks on the reflectance of DBRs has been explored theoretically and experimentally. The results show that AlN/Al_2O_3 DBRs with 11.5 pairs can achieve 96 % of reflectance. The stopband bandwidth covers from 720 to 880 nm. The surface roughness is around 2.9 nm with an area of 9 μm^2. Our sputtering-grown AlN/Al_2O_3 DBR with high reflectance and low surface roughness has laid a good foundation for the potential application of high-performance and rapid thermal dissipation DBRs in photonic integrated circuits.

1. Introduction

Aluminum Nitride (AlN) has gained significant attention in recent years due to its exceptional properties such as a wide bandgap of 6.1 eV [1], high thermal conductivity ~320 W m^{-1} K^{-1} [2], a critical field of ~15 MV cm^{-1} [3], electron mobility larger than 300 cm^2 V^{-1} s^{-1} [4], excellent chemical stability, and notable piezoelectric coefficients, making it a promising material in power electronics, photonics, and optoelectronics [5–8].

Due to high thermal conductivity and electrical insulation, AlN is an ideal substrate and heat sink for high-power devices in electronics [9]. Besides, the piezoelectric properties are exploited in bulk acoustic wave (BAW) filters which are essential components in modern communication systems [10]. Additionally, due to its transparency in the deep UV range, AlN is suitable for UV light-emitting diodes (LEDs) and laser diodes [11]. Also, the compatibility of AlN with III-nitride materials facilitates the development of high-efficiency UV optoelectronic devices [12].

Furthermore, Distributed Bragg Reflectors (DBRs), composed of alternating layers of dielectric materials with differing refractive indices, are critical in various optical and optoelectronic applications, including vertical-cavity surface-emitting lasers (VCSELs) and optical filters [13,14]. DBRs composed of organic-inorganic hybrid material and metal halide perovskite material are promising in solution-processed quantum dot light-emitting diodes [15,16]. DBRs built by dielectric materials such as Si–SiO_2, SiO_2/Ta_2O_5, SiO_2/TiO_2, SiO_2/HfO_2, and Al_2O_3/TiO_2 has been extensively studied [17–24]. Particularly, SiO_2/-TiO_2 DBRs are the commonly used due to their high refractive index contrast, leading to excellent reflectivity. However, they have disadvantages such as lower thermal conductivity (SiO_2 ~1.4 W m^{-1} K^{-1} and TiO_2 ~8.4 W m^{-1} K^{-1}) [25,26], lattice mismatch with III-nitrides, and potential optical absorption of TiO_2, which limit their potentials in some photoelectric devices. DBRs composed of AlN/Al_2O_3 are more advantageous than DBRs composed of SiO_2/TiO_2 due to their higher thermal conductivity, better optical performance in the UV range and better lattice matching with III-nitride semiconductors. These properties enhance thermal management and structural integrity in high-power and high-temperature applications, making AlN/Al_2O_3 DBRs more suitable for integration into devices like LEDs and laser diodes.

* Corresponding author. School of Physics and Astronomy, Cardiff University, Cardiff, CF24 3AA, United Kingdom.
E-mail address: Houb6@cardiff.ac.uk (B. Hou).

https://doi.org/10.1016/j.optmat.2025.117332
Received 22 April 2025; Received in revised form 25 June 2025; Accepted 16 July 2025
Available online 18 July 2025
0925-3467/© 2025 The Authors. Published by Elsevier B.V. This is an open access article under the CC BY license (http://creativecommons.org/licenses/by/4.0/).

In this work, we report on AlN/Al_2O_3 DBRs fabricated on an amorphous glass substrate via the RF sputtering technique. We show near unity reflectivity for a DBR optimised for near-IR wavelengths. The bandwidth of stopband of the DBRs is from 720 to 880 nm with bragg wavelength around 790 nm. The purpose of design of fabrication of the AlN/Al_2O_3 DBRs is to use as an optical cavity to enhance the optical performance of the near infrared heavy metal free colloidal quantum dots (QDs) and explore their applications in optical communication system, which will be more suitable due to their higher thermal conductivity than that of commonly used SiO_2/TiO_2 DBRs. AFM, SEM and X-ray diffraction measurements confirm the material quality of the deposited layer is high.

2. Results and discussion

2.1. AlN/Al_2O_3 DBRs preparations

For the deposition of AlN, nitrogen (N_2) and argon (Ar) are used as plasma source with ratio (N_2/Ar) of 7 %. The power is kept at 280 W, the pressure is maintained at ~2 mtorr, and deposition time is fixed at ~3600 s. For the deposition of Al_2O_3, argon (Ar) is used as plasma source. The power is kept at 100 W, the pressure is maintained at ~6 mtorr, and deposition time is fixed at ~4000 s. The growth rate of AlN is around 1.63 nm/min and 1.8 nm/min for Al_2O_3. The overall time spent on fabrication of 11.5 periods DBR is 24.2 h.

2.2. Simulation and optical properties of AlN/Al_2O_3 DBRs

The inset to Fig. 1(A) shows the structure of the DBR on an amorphous glass substrate with alternating quarter-wavelength thick layers of AlN/Al_2O_3. The thickness of AlN and Al_2O_3 are 98 and 120 nm, respectively, which are obtained by fitting the experimental results into simulation results. The simulation is carried out via MATLAB code using the transfer matrix method [27]. The designed Bragg wavelength is around 790 nm for near-infrared applications. To enhance the accuracy of the simulation, AlN and Al_2O_3 single layers are deposited separately on a glass substrate to measure the refractive index. The refractive index spectrum of AlN and Al_2O_3 is measured by spectroscopic ellipsometer (SEMILAB SE-2000) and is shown in Fig. 2. The results indicate that the wavelength dispersion of AlN is larger than that of Al_2O_3. The refractive index measured has been used in simulation. The related input parameters and output results are summarized in Table 1. Moreover, with the increase of the number of pairs (N_P) of DBR, the reflectivity of the design wavelength approached unity, as shown in Fig. 1(A). As shown in Fig. 1

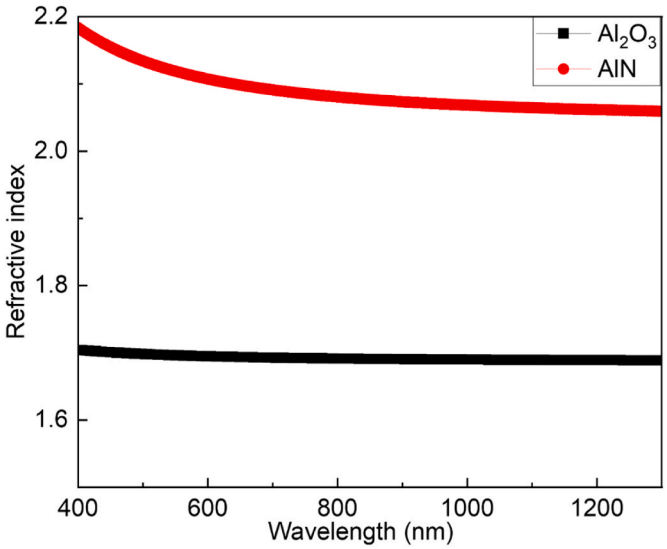

Fig. 2. The refractive index spectrum of AlN and Al_2O_3. AlN and Al_2O_3 thin flims are deposited on glass substrate and measured separately.

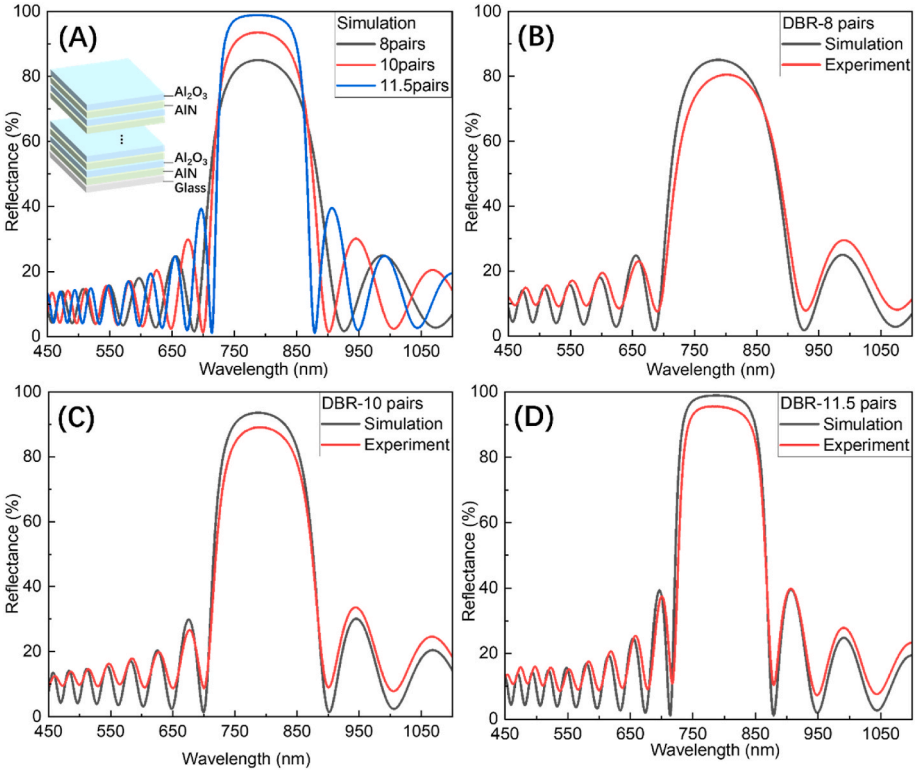

Fig. 1. (A) The simulation results of reflectance of AlN/Al_2O_3 DBRs with 8, 10, 11.5 pairs. The inset in Fig. 1(A) is the device structure of DBRs. Fig. 1(B–D) is the comparison of simulation results and experiment results for AlN/Al_2O_3 DBRs with 8, 10, 11.5 pairs, respectively.

Table 1
The parameters of DBRs simulated by transfer matrix method.

DBR Parameters	Simulation	Experiment
n[a]-AlN	2.06	2.06
n-Al_2O_3	1.63	1.63
n-air	1.0	1.0
n-glass	1.5	1.5
Incidence angle (degree)	0	0
Bragg wavelength (nm)	~790	~790
N_P[b] = 11.5	99 %	96 %
N_P = 10	94 %	89 %
N_P = 8	85 %	81 %

[a] n refers to refractive index.
[b] Np refers to number of pairs of DBRs.

(B–D), with the increase of N_P, the simulation results are getting more consistent with the experimental results which are measured by an integrating sphere in a PVE300 photovoltaic characterization system (Bentham). For example, when $N_P = 8$, the waveform of the reflectance spectrum from the experiment has a slight bias from that of simulation, as shown in Fig. 1(B). The relatively low reflectance and interface scattering loss should be responsible for this: the amplification of photos from reflectance cannot overcome the effect of interface scattering loss. However, when N_P further increases ($N_P \geq 10$), waveforms of the reflectance spectrum from the experiment and simulation become more consistent. This means that enhanced reflectance can overcome the effect of interface scattering loss.

Furthermore, the peak reflectance of DBRs with different N_P from the experiment is slightly smaller than that of the simulation, as shown in Fig. 1(B–D). This can be attributed to the sub-bandgap resonant absorption originating from material imperfections such as defect states [28], interface roughness and surface scattering. Fig. S1 shows the transmittance spectrum for both samples and the bandgap of AlN is estimated to be ~5.7 eV which is consistent with previous reports [29, 30]. However, compared to epitaxial-grown AlN with bandgap of ~6.1 eV [31] the slightly smaller bandgap for our AlN suggests the presence of defects in the film [31]. Besides, with the increase of DBR stacks, the defects will be accumulated. The defect states will contribute to the sub-bandgap resonant absorption leading to the consumption of photons and reducing reflectance. This can be further confirmed via the absorbance and absorptance spectrum, as shown in Fig. 3. It shows that the absorbance and the absorptance in the bandwidth region are from around 720 to 880 nm in consistency with the bandwidth of stopband, increasing with the increase of N_P. The increase of N_P leads to an increase in the reflectance. Therefore, more photons satisfying the requirement of the Bragg condition will be confined in the materials which contribute to sub-bandgap resonant absorption due to the defect states, as more obviously shown in Fig. 3(D). The absorption coefficient and extinction coefficient derived from Fig. 3(D) are shown in Fig. S2 in detail. In the stopband region, the coefficients dominate and the values out of stopband region are small.

2.3. XRD, AFM and SEM analysis of AlN/Al_2O_3 DBRs

Crystallographic property of as-prepared AlN and Al_2O_3 is characterized by X-ray diffractometer (PANalytical X'pert Pro). For AlN and Al_2O_3 single-layer thin film, the results of the X-ray diffraction characterization reveal that AlN has a preferable growth orientation along the c-axis on an amorphous glass substrate and Al_2O_3 has an amorphous structure, as shown in Fig. S3. The possible growth mechanism will be elaborated later. The full width at half maximum (FWHM) is estimated to be 1314 arcsec for the single layer AlN on glass substrate. Fig. 4 shows the X-ray diffraction patterns of DBRs with 8, 10 and 11.5 pairs. Similar to the result of the single AlN layer, the diffraction pattern of DBR stacks originates from AlN, and as-prepared AlN still preserves preferable c-axis growth orientation with (0002) diffraction plane even on an amorphous Al_2O_3 layer. Besides, the intensity of the diffraction peak increases with DBR pairs and this is attributed to the constructive interference effect of AlN layers with preferable c-axis orientation in

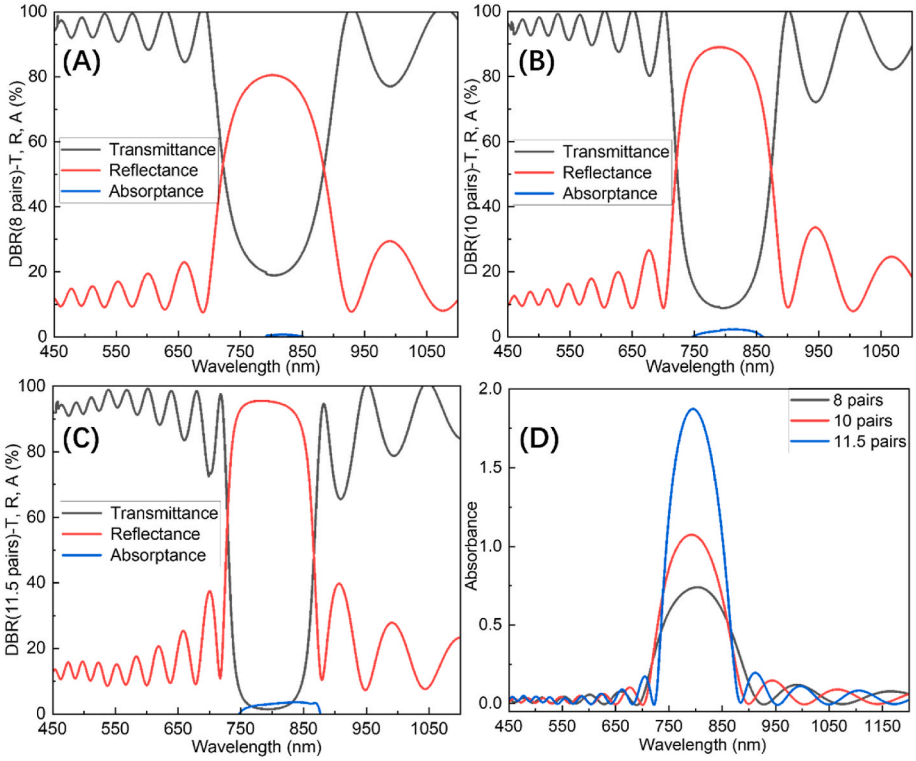

Fig. 3. The transmittance, reflectance and absorptance spectrum of (A) 8 pairs of DBR, (B) 10 pairs of DBR, and (C) 11.5 pairs of DBR. (D) The absorbance spectrum of 8, 10, 11.5 pairs of DBR.

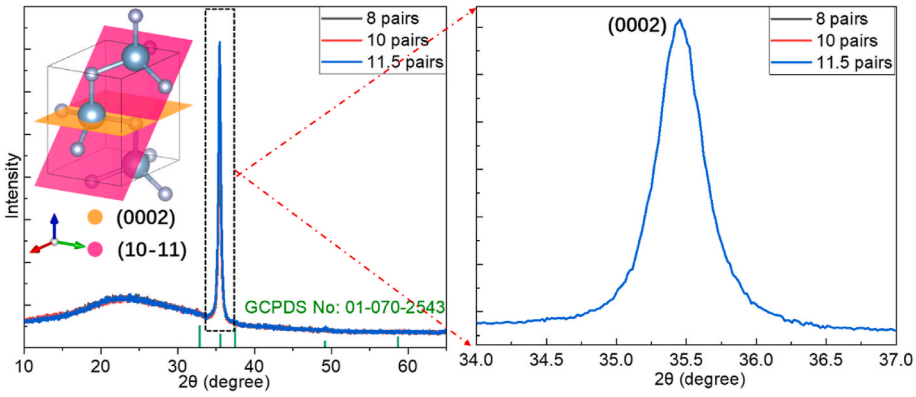

Fig. 4. X-ray diffraction patterns of AlN/Al_2O_3 DBRs with 8, 10 and 11.5 pairs. Left panel inset shows the details of diffraction pattern from 34° to 37°.

DBR stacks [32]. The diffraction peak position of AlN on the Al_2O_3 layer in DBRs and a single AlN layer on glass is the same, which is 35.5° (±0.1°). The FWHMs are 1375, 1386 and 1393 arcsec for DBRs with pairs of 8, 10 and 11.8 respectively. Compared with FWHM of a single layer AlN, the increasement of FWHM is only 4.6 %, 5.5 % and 6.0 %, which is relatively small. This implies that our sputtering process of growing AlN/Al_2O_3 DBRs has the potential to transfer to other substrates such as silicon (Si), or silicon dioxide (SiO_2) or gallium nitride (GaN), which can lay a promising foundation for the applications in Si-based [33] or GaN-based integrated electronic and photoelectronic devices [34].

Notably, there are no satellite peaks observed in X-ray diffraction spectrum of AlN/Al_2O_3 DBRs. There are potential reasons for this. The diffraction peak is originated from AlN thin films in DBR stacks. There is no contribution from amorphous Al_2O_3 thin films to enhancement of diffraction peaks. Typically, the satellite peaks will appear when the quality of thin films is very good. Fig. S4(a) shows the intensity of diffraction peak of one layer AlN thin film on glass substrate. The intensity is not high and the FWHM is around 1314 arcsec, but the AlN thin films deposited on sapphire have FWHMs of ~200–~300 arcsec [37,38]. Comparatively, the quality of AlN on glass by RF sputter is not very good. Besides, with the incorporation of AlN films into AlN/Al_2O_3 DBRs, the intensity increases slightly from ~5000 to ~7000 due to the constructive interference as shown in Fig. S4(b). However, FWHMs also increase from 1375, 1386 and 1393 arcsec showing the quality of thin films is decreasing. This is owing to the accumulation of defects and strain in AlN films as well as interface scattering between films. Consequently, on glass substrate the AlN thin film without very good quality is prepared and then on that AlN thin film, AlN/Al_2O_3 DBRs is subsequently deposited. The quality of AlN quality degrades with increase of DBR stacks, which should be responsible for no satellite peaks being observed. Furthermore, the amorphous Al_2O_3 can compromise constructive interference and interface roughness increasing with the increase of DBR stacks from less than 1 nm–3 nm is another factor compromising constructive interference and broadening linewidth of the diffraction peaks. In summary, the lack of satellite peaks in X-ray diffraction spectrum of AlN/Al_2O_3 DBRs samples can be attributed to a synergy effect of defects, interface roughness and amorphous Al_2O_3. The defects in AlN films should be the major factor, the next is the interface scattering between AlN and Al_2O_3, and the last is the scattering from the amorphous Al_2O_3. AlN/Al_2O_3 DBRs with preferable c-axis growth orientation is not enough to generate satellite peaks in X-ray diffraction patterns.

Besides, achieving AlN with preferable growth orientation along the c-axis on amorphous glass substrate via RF sputtering process should satisfy certain deposition conditions such as relatively high sputtering power, low chamber pressure and short target substrate distance. The AlN prepared is a hexagonal crystal and has a diffraction peak in (0002) plane which belongs to {0001} family that has the highest surface energy among other families of crystal plane such as {1–100} and {11–20} [39]. If the growth of AlN film governs by thermodynamics which directs that growth of crystal obeys the principle of minimum energy such as minimum surface energy. Then the preferable growth orientation should be along one of directions from {1–100} family since the surface energy is the minimum. However, our experimental data shows that the prepared wurtzite AlN has a preferable orientation along [0001]. This means that besides thermodynamic process another important growing mechanism, which is the kinetic process, dominates during growth of AlN. The kinetic process involves how fast atoms attach to the surface of substrate and how fast atoms move on the surface of substrate. This requires atoms need to have enough energy to attach to substrate to form crystal nucleation. On the other hand, atoms should have energy to migrate on the surface to reconstruct the surface so that more closely packed (0002) plane can be grown. Therefore, the picture of AlN growing process can be depicted as follows: Firstly, at early stage of nucleation, crystal nucleation of AlN with different orientations are formed on the substrate. Later, under the control of thermodynamics, crystal planes (such as {1–100} and {11–20} planes) grow very fast due to their low surface energies. However, it's because of their fast-growing process that they quickly collide with neighboring grains. This can lead to a consequence that their surfaces are no longer exposed to incoming flux and finally their growing process can be cut off by neighboring grains. For crystal nucleation with (0002) plane, under governing of thermodynamics it hardly grows due to high surface energy, however, since the energy of atoms are so high enough that it can overcome the surface energy barrier and it will rearrange on the substrate surface and continues to grow under the governing of kinetics of crystal growth. High sputtering power can supply atoms with high energy. Low chamber pressure makes sure longer mean free path and no dissipation of energy of atoms due to less collision with other atoms. Short distance between substrate and target guarantees atoms with the mean free path can quickly attach to substrate surface, migrate and rearrange. This is the possible mechanism of deposition of AlN with preferable c-axis orientation via sputtering process.

Additionally, surface roughness of as-prepared DBRs is mapped by atomic force microscope (Bruker AFM ScanAsyst). Fig. 5(A–C) show the atomic force microscopic images of DBRs with 8, 10 and 11.5 pairs, which are terminated by Al_2O_3, Al_2O_3 and AlN, respectively. Fig. S5 shows the AFM image of DBRs with 12 pairs. The result shows that the surface roughness (R_{rms}) tends to increase with the increase of N_P. However, when the value of N_P is 11.5, R_{rms} remain relatively low with a value of 2.93 (±0.05) nm which is very close to 2.86 (±0.05) nm for the sample with $N_P = 8$. This means that DBRs terminated by the AlN layer are capable of achieving a low surface roughness, and it might be attributed to the preferable c-axis orientation growth of AlN via sputtering process. For a single layer AlN thin film and a single layer Al_2O_3 thin film deposited on glass substrate, the atomic force microscope images show that the surface roughness is 0.5 (±0.05) nm for AlN and 0.8

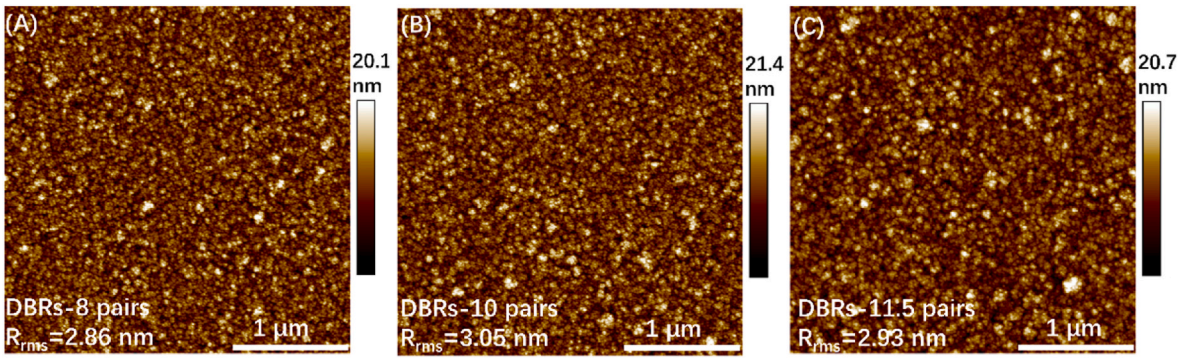

Fig. 5. Atomic force microscopic images of DBRs with 8 (A), 10 (B) and 11.5 (C) pairs.

(±0.05) nm for Al_2O_3 over an area of 9 μm^2, as shown in Fig. S6. Compared with the surface roughness of a single AlN layer on a glass substrate with R_{rms} of 0.5 nm, the value of R_{rms} around 2.9 nm for 11.5 pairs of DBRs is relatively larger, but it is still a good result which is beneficial for applications in photonic and optoelectronic devices [35]. It is worth noting that with the increase of DBR stacks, the R_{rms} tends to increase. This can lead to reduce of reflectance due to interface scattering of photons. This is one origin for the mismatch of reflectance between simulation result and experimental result. In addition, for the effect of surface scattering on reflectance, the effect of diffuse reflection and specular reflection on reflectance has been explored as shown in Fig. S7. The contribution of specular reflection is the dominant mechanism to the high reflectance of DBRs. The contribution of diffuse reflection is very small, which further suggests the surface is relatively smooth. However the contribution of diffuse reflection is small, it can still scatter the photons and reduce the constructive interference which is another origin leading to the difference between simulation results and experimental results in reflectance.

To further explore the DBR stacks, cross-sectional cleavage images of as-prepared DBRs are mapped by scanning electron microscope (Hitachi Regulus 8230 SEM). Fig. 6 shows cross sectional scanning electron microscopic (SEM) images of AlN/Al_2O_3 DBRs with 8, 10 and 11.5 pairs, from which the AlN/Al_2O_3 stacks can be observed clearly. The samples are cut by a diamond cutter and then broken apart manually. A small amount of gold particles is deposited on the cleaved surface to avoid charging effect during image collection. However, these makes it a little difficult to clearly distinguish the interfaces between AlN and Al_2O_3. Overall, the images show the layers are flat, over the scale of microns. Besides, the pillar structure in the images is an AlN layer due to the property of preferable c-axis growth orientation. The SEM energy dispersive spectroscopy (EDS) line-scan plot of a DBRs with N_P of 11.5 further provides a solid proof that the alternating AlN/Al_2O_3 structure is well stacked in DBRs as shown in Fig. 6(D). The sharp vertical side wall plot for the line scan has not been observed, this might be attributed to three factors: one is the blocking effect from deposited gold particles; the next one is the limited resolution of the detectors for both oxygen and nitrogen; the last one is the effect of interface roughness which increases with the deposition of DBR stacks and this can be proved from results of AFM measurements. However, the periodicity still can be extracted from the line-scan plot and the value is about 220 nm which is consistent 218 nm from the fitting between simulation result and experimental result.

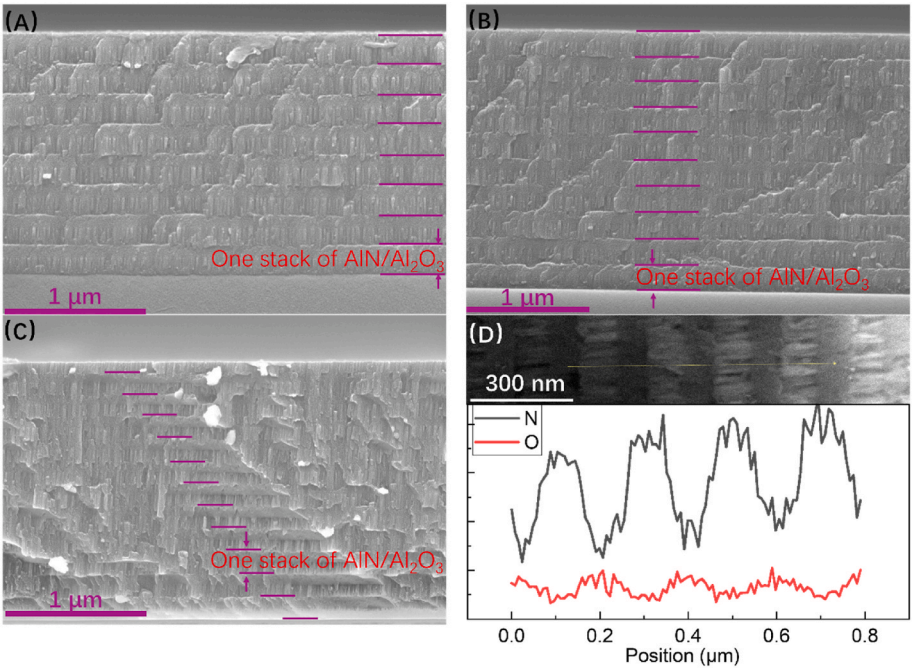

Fig. 6. (A–C) Scanning electron microscopic (SEM) images of DBRs with 8, 10 and 11.5 pairs. (D) Energy dispersive spectroscopy (EDS- SEM) line-scan plot of the DBR with N_P of 11.5.

2.4. The angular dependent reflectance of AlN/Al_2O_3 DBRs

Angular dependent transmittance and absorbance are measured by UV–Vis–NIR Spectrophotometer (Agilent Cary 7000 UMS). Fig. 7(A–C) shows the angular dependent reflectance of 8, 10 and 11.5 pairs of DBRs with s-polarized incident light, and the incident angle varied from 5.1° to 70°. We can observe from Fig. 7(A–C) that the reflectance increases with the incident angle for s-polarized light (s-light).

For s-light (electric field perpendicular to the plane of incidence), the reflectance at an interface between two dielectric materials is given by the Fresnel equation, which we can find in any optics textbook [36]:

$$R_s = \left| \frac{n_1 cos\,\theta_i - n_2 cos\,\theta_t}{n_1 cos\,\theta_i + n_2 cos\,\theta_t} \right|^2 \quad (1)$$

where R_s is reflectance for s-light, n_1 and n_2 are refractive indices of alternating layers, θ_i is the incident angle, and θ_t is the transmitted angle. The relationship between θ_i and θ_t is from Snell's law:

$$n_1 sin\,\theta_i = n_2 sin\,\theta_t \quad (2)$$

Therefore, with an increase of θ_i, the denominator of equation (1) gets smaller, leading to an increase of R_s. This means that for s-light at higher incident angles, more light is reflected.

Besides, the Bragg wavelength is shifting to a lower value with increased incident angles for s-light. This can be explained via Bragg condition:

$$m\lambda = 2 d_{eff} n_{eff} cos\,\theta_t \quad (3)$$

where m is the order of reflection, λ is the centre wavelength of reflection, d_{eff} is the effective optical thickness of each layer, and n_{eff} is the effective refractive index. Based on equations (2) and (3), as θ_i increases, the optical thickness of each layer effectively decreases, shifting the high-reflectance band to shorter wavelengths.

Fig. 7(D–F) shows the angular dependent reflectance of 8, 10 and 11.5 pairs of DBRs with p-polarized incident light (p-light, electric field within the plane of incidence) and incident angles vary from 5.1° to 70°. The Bragg wavelength is also shifting to a lower value with the increase of incident angle for p-light. The interpretation is the same as s-light. However, the reflectance tends to decrease with an increase of incident angles to Brewster's angle and slightly increases after passing Brewster's angle. This can be explained by the Fresnel equation and Brewster's angle condition for p-light (electric field parallel to the plane of incidence):

$$R_p = \left| \frac{n_1 cos\,\theta_t - n_2 cos\,\theta_i}{n_1 cos\,\theta_t + n_2 cos\,\theta_i} \right|^2 \quad (4)$$

$$\theta_B = tan^{-1} \frac{n_2}{n_1} \quad (5)$$

where R_p is reflectance for p-light, when θ_i increases to θ_B, R_p gradually decreases based on equation (4). When θ_i equals θ_B, R_p is 0 due to the 2 terms in the numerator of (4) being equal to each other. After Brewster's angle, the numerator is not 0. Therefore, R_p gradually increases. For Fig. 7(D–E), since DBRs are terminated with Al_2O_3, the θ_B is around 58.5°. Therefore, we can observe reflectance increases after 60°.

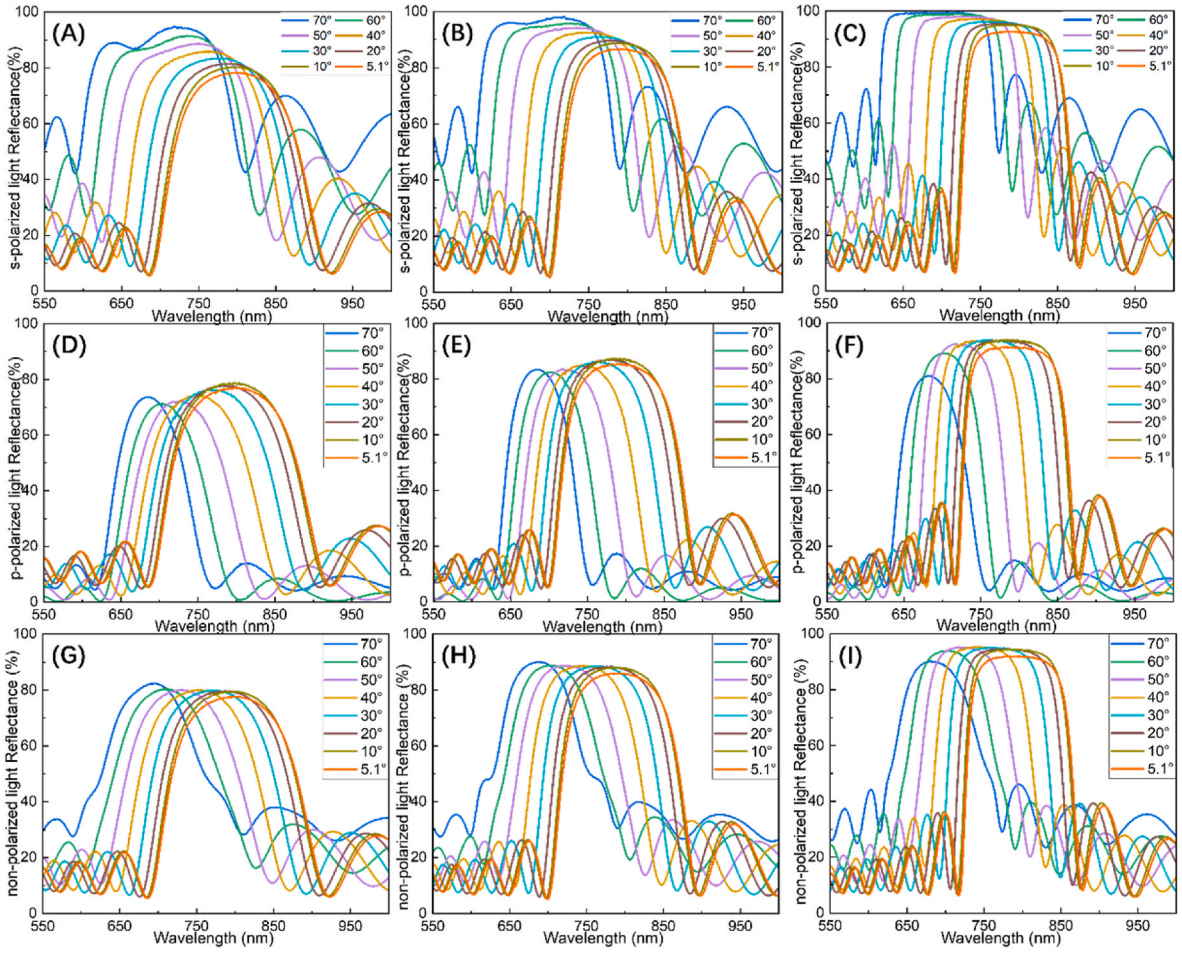

Fig. 7. (A–C) s-polarized light angular dependent of reflectance of DBRs with 8, 10, 11.5 pairs. (D–F) p-polarized light angular dependent of reflectance of DBRs with 8, 10, 11.5 pairs. (G–I) Non-polarized light angular dependent of reflectance of DBRs with 8, 10, 11.5 pairs.

However, for Fig. 7(F), since DBR is terminated by AlN, the θ_B is around 64° located between 60° and 70°, but reflectance at 70° is smaller than 60°. Therefore, we can see that reflectance decreases with increase of θ_i.

For Fig. 7(G–I), the non-polarized light reflectance is calculated by the average value of s-light and p-light at different θ_i for DBRs, therefore the non-polarized light reflectance is determined by the reflectance of s-light and p-light. In summary, for DBR with NP of 11.5, it can achieve a very high reflectance with incident angles ranging from 10 to 50°.

3. Conclusions

For the first time, we have achieved AlN/Al_2O_3 DBRs with excellent optical and morphological performances via the RF sputtering process on glass at room temperature. The result shows that the bandwidth of DBRs narrows with the increased pairs of DBRs. Besides, it also shows that the AlN layer in DBR stacks has a preferable c-axis orientation, and the DBR terminated by the AlN layer has lower surface roughness which is 2.9 nm. The high reflectance with an index of 96 % and good performance of angular dependent reflectance of the AlN/Al_2O_3 DBR has many potential applications in photonics and optoelectronics.

CRediT authorship contribution statement

Renjun Liu: Writing – review & editing, Writing – original draft, Visualization, Methodology, Investigation, Formal analysis, Data curation. **Chandra Kant:** Investigation, Data curation. **Hüseyin Bilge Yağcı:** Investigation, Formal analysis, Data curation. **Haifeng Qi:** Formal analysis, Data curation. **Hong Ji:** Visualization, Investigation. **William Solari:** Investigation. **Sri Datta Aneesh Chodavarapu:** Investigation, Formal analysis. **Benxuan Li:** Investigation. **Sheng Wang:** Writing – review & editing. **Anthony J. Bennett:** Writing – review & editing, Validation, Data curation. **Ning Zhang:** Writing – review & editing, Resources, Funding acquisition. **Ingo Ludtke:** Writing – review & editing, Resources, Funding acquisition. **Wenlong Ming:** Writing – review & editing, Resources, Funding acquisition. **Bo Hou:** Writing – review & editing, Writing – original draft, Validation, Supervision, Methodology, Investigation, Funding acquisition, Conceptualization.

Declaration of competing interest

The authors declare the following financial interests/personal relationships which may be considered as potential competing interests: Bo Hou reports a relationship with Cardiff University that includes: employment. If there are other authors, they declare that they have no known competing financial interests or personal relationships that could have appeared to influence the work reported in this paper.

Acknowledgements

The authors acknowledge the financial support from the EPSRC SWIMS (EP/V039717/1) and Leverhulme Trust (RPG-2022-263). B. H. and I.L. thanks the financial support from a collaboration with Compound Semiconductor Applications Catapult, funded by the Engineering and Physical Sciences Research Council's Innovation Launchpad Network + Researcher in Residence scheme (EP/W037009/1, EP/X528493/1). B.H. and W.L.M. thank the financial support from the Welsh Government Sêr Cymru programme - Enhancing Competitiveness Equipment Award 2022/23 (MA/VG/2715/22-PN66).

Appendix A. Supplementary data

Supplementary data to this article can be found online at https://doi.org/10.1016/j.optmat.2025.117332.

Data availability

Information on the data underpinning this publication, including access details, can be found in the Cardiff University Research Data Repository at [DOI: 10.17035/cardiff.28784888].

References

[1] J.Y. Tsao, et al., Adv. Electron. Mater. 4 (2018) 1600501.
[2] R.R. Sumathi, ECS J. Solid State Sci. Technol. 10 (2021) 035001.
[3] W.A. Doolittle, et al., Appl. Phys. Lett. 123 (2023) 070501.
[4] P. Bagheri, et al., J. Appl. Phys. 132 (2022) 185703.
[5] T.P. Chow, I. Omura, M. Higashiwaki, H. Kawarada, V. Pala, IEEE Trans. Electron. Dev. 64 (2017) 856.
[6] Y. Taniyasu, M. Kasu, T. Makimoto, Appl. Phys. Lett. 85 (2004) 4672.
[7] T.-J. Lu, et al., Opt. Express 26 (2018) 11147.
[8] W. Sun, C.-K. Tan, N. Tansu, Sci. Rep. 7 (2017) 11826.
[9] S. Yin, K.J. Tseng, J. Zhao, Appl. Therm. Eng. 52 (2013) 120.
[10] Y. Zou, et al., Microsys. Nanoeng. 8 (2022) 124.
[11] S. Zhao, et al., Sci. Rep. 5 (2015) 8332.
[12] A. Pandey, W.J. Shin, J. Gim, R. Hovden, Z. Mi, Photon. Res. 8 (2020) 331.
[13] C. Zhang, H. Li, D. Liang, Nat. Commun. 15 (2024) 1105.
[14] Y. Horie, A. Arbabi, E. Arbabi, S.M. Kamali, A. Faraon, Opt. Express 24 (2016) 11677.
[15] X.-B. Shi, Y. Hu, B. Wang, L. Zhang, Z.-K. Wang, L.-S. Liao, Adv. Mater. 27 (2015) 6696.
[16] R. Liu, H. Ji, D.M. Othman, A.R.C. Osypiw, W. Solari, W. Ming, J.I. Sohn, J.C. Shin, B. Hou, InfoScience (2025) e12027, 2(1).
[17] Y. Jiang, D. You, Y. Cao, W. Guo, M. Tan, Vacuum 220 (2024) 112775.
[18] Z.-S. Yuan, J.-M. Jhang, P.-H. Yu, C.-M. Jiang, Y.-C. Huang, Y.-L. Wu, J.-J. Lin, C.-F. Yang, Vacuum 182 (2020) 109782.
[19] T. Sakai, M. Kushimoto, Z. Zhang, N. Sugiyama, L.J. Schowalter, Y. Honda, C. Sasaoka, H. Amano, Appl. Phys. Lett. 116 (2020) 122101.
[20] J. Liu, C.-Y. Lin, W.-C. Tzou, N.-K. Hsueh, C.-F. Yang, Y. Chen, Cryst. Growth Des. 18 (2018) 5426.
[21] F. Réveret, et al., J. Appl. Phys. 120 (2016) 093107.
[22] L. Lv, Y. Shuai, S. Huang, D. Zhu, Y. Wang, W. Luo, C. Wu, W. Zhang, ACS Omega 7 (2022) 20994.
[23] M. Hála, R. Vernhes, O. Zabeida, J.-E. Klemberg-Sapieha, L. Martinu, J. Appl. Phys. 116 (2014) 213302.
[24] I.W. Feng, S. Jin, J. Li, J. Lin, H. Jiang, J. Vac. Sci. Technol. A 31 (2013) 061514.
[25] X. Feng, X. Wang, X. Chen, Y. Yue, Acta Mater. 59 (2011) 1934.
[26] W. Zhu, G. Zheng, S. Cao, H. He, Sci. Rep. 8 (2018) 10537.
[27] V. Filonov, Y. Filonova, Y. Dubyk, E. Pis'mennyi, Int. J. Heat Mass Tran. 187 (2022) 122531.
[28] S. Kim, S.-H. Lee, I.H. Jo, J. Seo, Y.-E. Yoo, J.H. Kim, Sci. Rep. 12 (2022) 5124.
[29] R. Liu, et al., in: 2024 IEEE Workshop on Wide Bandgap Power Devices and Applications in Europe (Wipda Europe), 2024, p. 1.
[30] R.M.R. Pinto, V. Gund, C. Calaza, K.K. Nagaraja, K.B. Vinayakumar, Microelectron. Eng. 257 (2022) 111753.
[31] Q. Zhou, Z. Zhang, H. Li, S. Golovynskyi, X. Tang, H. Wu, J. Wang, B. Li, APL Mater. 8 (2020) 081107.
[32] S. Liu, M. Peng, C. Hou, Y. He, M. Li, X. Zheng, Nanoscale Res. Lett. 12 (2017) 279.
[33] M. Nong, C.-H. Liao, X. Tang, H. Cao, T. Liu, P.A.M. Cortez, D. Chettri, G.I. M. García, X. Li, Appl. Phys. Lett. 124 (2024) 172107.
[34] T.H. Park, T.H. Lee, T.G. Kim, J. Alloys Compd. 776 (2019) 1009.
[35] B. Li, Y. Wang, A. Birge, B. Kim, X. Fang, M.L. Lee, IEEE J. Photovoltaics 15 (2025) 87.
[36] P. Ewart, The Science of Light, Morgan & Claypool Publishers, 2019.
[37] D.D. Koleske, J.J. Figiel, D.L. Alliman, B.P. Gunning, J.M. Kempisty, J. R. Creighton, A. Mishima, K. Ikenaga, Appl. Phys. Lett. 110 (2017) 23.
[38] X. Zhang, et al., CrystEngComm 17 (2015) 39.
[39] D. Holec, P.H. Mayrhofer, Scr. Mater. 67 (2012) 9.